Simulation of single fiber dynamics

Paal Skjetne
Department of Chemical Engineering, University of Wisconsin-Madison, Madison, Wisconsin, 53706 and Department of Physics, Norwegian University of Science and Technology, N-7034 Trondheim, Norway

Russell F. Ross
Department of Engineering Mechanics and Astronautics, University of Wisconsin-Madison, Madison, Wisconsin, 53706

Daniel J. Klingenberg[a)]
Department of Chemical Engineering and Rheology Research Center, University of Wisconsin-Madison, Madison, Wisconsin, 53706

(Received 18 March 1997; accepted 6 May 1997)

Simulation results for the motion of flexible fibers modeled as rigid spheres connected by ball and socket joints are presented. Simulations of isolated stiff fibers reproduce such features of Jeffery orbits as orbit stability, the dependence of the dimensionless orbit period on only the fiber aspect ratio (independent of shear rate and orientation), and trajectories identical to those of prolate spheroids of the same equivalent aspect ratio. Simulations of stiff fibers ''pole-vaulting'' near a bounding surface qualitatively reproduce experimental observations. Fiber trajectories are very sensitive to the short-range interactions between a fiber and a bounding surface. In contrast to rigid fibers, flexible fiber orientations drift in unbounded simple shear and parabolic shear flows. The drift direction and rate depend on fiber stiffness, initial orientation, as well as the ambient flow field. A wide variety of configurational dynamics are observed, which also depend on the fiber stiffness, initial orientation, and the ambient flow field. These results agree with previous experimental observations of flexible fibers in shear flows. © *1997 American Institute of Physics.* [S0021-9606(97)52330-0]

I. INTRODUCTION

The translational and rotational dynamics of rigid and flexible fibers are important in a variety of diverse fields. Fiber orientation and spatial distributions play a significant role in such properties of fiber-reinforced composites as elastic moduli, thermal and electrical conductivities, and thermal expansivities. In pulp and paper processing, fiber dynamics and microstructure evolution during the sheet forming process are among the most important factors controlling such properties as sheet strength and optical characteristics. Many previous investigations of fiber dynamics, both experimental and theoretical, have focused on the dynamics of rigid fibers, while relatively little attention has been paid to the more complicated dynamics of flexible fibers. In a previous paper[1], we presented a mechanical model for flexible fibers and a simulation technique for studying their dynamics in flowing suspensions. The purposes of this paper are to verify that the model and simulation method accurately reproduce a wide variety of theoretical predictions and experimental observations of isolated rigid and flexible fiber dynamics, and to illustrate some of the complicated dynamics of flexible fibers.

Jeffery[2] analyzed the motion of ellipsoids in uniform, creeping shear flow in a Newtonian fluid. For a prolate spheroid of aspect ratio a_r ($\equiv$ major axis length $2a$/minor axis length $2b$) in an ambient simple shear flow, $\mathbf{U}^{\infty}=(\dot{\gamma}y,0,0)$, the angular motion of the spheroid is described by

$$\tan\theta=\frac{Ca_r}{\sqrt{a_r^2\cos^2\phi+\sin^2\phi}}, \tag{1}$$

$$\tan\phi=a_r\tan\left(2\pi\frac{t}{T}\right), \tag{2}$$

where θ is the angle between the fiber's major axis and the vorticity axis (Z axis), ϕ is the angle between the Y-axis and the XY-projection of the fiber axis (see Fig. 1), T is the orbit period,

$$T=\frac{2\pi}{\dot{\gamma}}\left(a_r+\frac{1}{a_r}\right), \tag{3}$$

and C is the orbit constant, determined by the initial orientation,

$$C=\tan\theta_0\sqrt{\cos^2\phi_0+\frac{1}{a_r^2}\sin^2\phi_0}.$$

This analysis predicts that a prolate spheroid will repeatedly rotate through the same orbit, that the orbit period is independent of the initial orientation or orbit constant C, and that the particle will not migrate across streamlines.

To compare experimental observations with Jeffery's predictions, it is convenient to observe a spheroid's projection in the XY, XZ or YZ planes. The spheroid projection on the XZ plane rocks back and forth about the Z axis to a maximum angle λ_{xz},[3] where

$$\tan\lambda_{xz}=Ca_r. \tag{4}$$

[a)]Electronic mail: klingen@neep.engr.wisc.edu

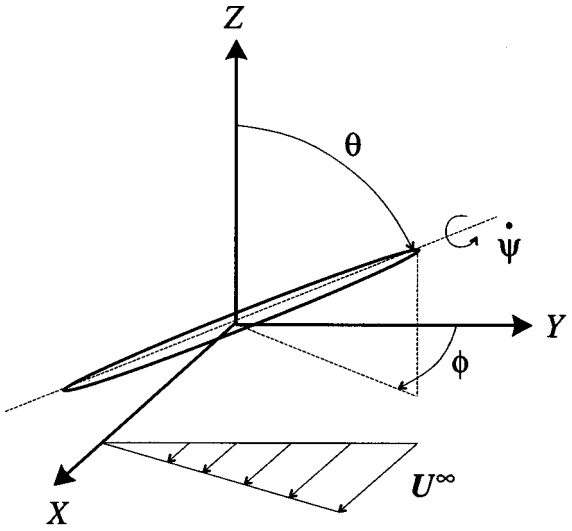

FIG. 1. Schematic diagram defining the orientation of a prolate spheroid in a uniform shear flow.

λ_{xz} approaches $\pi/2$ as $C\to\infty$, where the fiber rotates entirely in the XY plane. The spheroid projection on the YZ plane also rocks back and forth about the Z axis, to a maximum angle $\lambda_{yz}=\tan^{-1}C$.

While the spheroid rotates in its elliptic orbit, it also spins around its major axis with an angular velocity $\dot{\psi}=(\dot{\gamma}/2)\cos\theta$. Experimentally monitoring $\dot{\psi}$ is very challenging. A more accessible measure is the number of axial spins, n, completed during one rotational period[4,5]

$$n=\frac{2}{\pi}\int_0^{\frac{T}{4}}\dot{\psi}(t)dt=\frac{a_r^2+1}{\pi a_r\sqrt{C^2a_r^2+1}}K(k), \tag{5}$$

where $k=\sqrt{C^2(a_r^2-1)/(C^2a_r^2+1)}$ and $K(k)=\int_0^{\pi/2}d\zeta(1-k^2\sin^2\zeta)^{-1/2}$ is the complete elliptic integral of first kind.

Bretherton[6] showed that Jeffery's analysis is valid for any axisymmetric particle. For axisymmetric shapes other than prolate spheroids, however, the aspect ratio is replaced by an equivalent aspect ratio a_{r_e} defined in terms of the actual period T via Eq. (3). Chwang[7] showed that Jeffery's analysis also applies for prolate spheroids in quadratic, paraboloidal flows, provided that the shear rate $\dot{\gamma}$ is replaced by the ambient shear rate evaluated at the particle center. Yarin *et al.*[8], however, have recently shown that some nonaxisymmetric elongated bodies deviate from Jeffery's predictions, exhibiting chaotic orientation dynamics.

The dynamics of flexible fibers are significantly more complicated. Much of the current knowledge of flexible fiber dynamics has come from the experimental observations of Mason and co-workers.[4,9,10] Arlov *et al.*[9] divided their experimental observations of flexible fiber dynamics into three classifications.

(i) **Group 1** (''flexible spin''). Fibers nominally oriented along the vorticity axis spun about this axis, and bent into arcs. The maximum curvature occurred when the plane of the arc was in the XZ plane, and the minimum curvature occurred when the arc was in the YZ plane.

(ii) **Group 2** (''flexible spin-rotation''). Here fibers exhibited the flexible spin defined above, superimposed on an elliptic orbit. The likelihood of this motion decreased with increasing flexibility.

(iii) **Group 3**. This most common classification was divided into three sub-groups. All fibers in this class nominally aligned with the X axis when rotating through the XZ plane.

Group 3A (''springy rotations''). While rotating in the XY plane, a fiber bent like a leaf spring when the ends were in the second and fourth quadrants, and straightened out when aligned with the flow.

Group 3B (''snake turn''). We refer to this type of motion as a *U turn*. This type of dynamics was exhibited by more flexible fibers than those in group 3A. Initially, these fibers were aligned along the X axis and appeared straight when viewed along the Y axis. One end would start bending in the XY plane, and the bend would move from the leading end of the fiber to the other, then straighten out in the course of a half period. For longer fibers, the leading end would start bending again before the fiber straightened out.

Group 3C (''S-turns''). These types of motions were observed for fibers whose major axes had a slight curvature in the XZ plane when aligned with the X axis. Starting from this orientation, both ends would start bending in opposite directions. The fiber would form an S shape when viewed along the Z axis, and a loop when viewed along the Y axis. We refer to this as an *S-loopturn*. Arlov *et al.* observed that some very uniform fibers would bend to form an S shape entirely in the XY plane. We call this a *pure S-turn*.

Arlov *et al.*[9] also observed that rigid fibers rotated in periodic orbits with constant C, but that for flexible fibers in Couette flow, the orbit constant drifted with time. For small C, the fibers tended to drift toward $C=0$, while for large C, the fibers tended to drift toward $C=\infty$. However, for a given initial orbit constant, drift was not always in the same direction, nor was the drift always monotonic. The authors speculated that the initial fiber orientation may play a role in the orbit constant drift. The fibers tended to reach their ultimate orbits at a rate that depended on the initial orientation.

Forgacs and Mason[4] examined the hydrodynamic forces acting to deform extensible flexible fibers in simple shear flow. The axial hydrodynamic force on a straight fiber at a constant shear rate was approximated as $F=\text{constant}\times M$, where the orientation factor M is

$$M=\frac{C^2a_{r_e}^2\sin\phi\cos\phi}{C^2a_{r_e}^2+a_{r_e}^2\cos^2\phi+\sin^2\phi}. \tag{6}$$

For $C=\infty$, the maximum compressive force occurs when the fiber is aligned with the principal axis of compression of the simple shear flow ($\phi=-45°$). As the orbit constant decreases, the maximum compressive force decreases and shifts toward orientations in the XZ plane. This suggests that

the dynamics of flexible fibers, particularly the bending and twisting motions, are expected to depend on the fiber orientation and conformation.

Investigations of flexible fibers are well-suited for simulation methods. Yamamoto and Matsuoka[11–14] developed a method for simulating such fibers in shear flow, where the fiber is modeled as a chain of rigid spheres connected through springs, with potentials to mimic resistance to bending and twisting. Chain connectivity is maintained by constraints, producing equations that must be solved iteratively and simultaneously with the equations of motion. This method has been shown to reproduce certain dynamics of isolated fibers[11], and has been employed to investigate the single fiber contribution to the suspension viscosity[12], flow-induced fiber fracture of isolated fibers[13], and fiber suspension behavior[14].

In a previous paper[1], we presented a different particle-level simulation method for the structural evolution of flexible fiber suspensions in shear flow. The fiber model is similar to that used by Yamamoto and Matsuoka[11], except that the fiber was modeled as an inextensible chain of rigid prolate spheroids connected through ball and socket joints. This model eliminates the need for iterative constraints to maintain fiber connectivity, and can represent large-aspect ratio fibers with relatively few bodies. These features help to reduce computations, facilitating simulation of concentrated suspensions[1].

The purposes of the present paper are to verify that the model developed in Ref. 1 reproduces a wide variety of theoretical predictions and experimental observations of flexible fiber dynamics as described above, and to illustrate the complicated dynamics of flexible fibers. In Sec. II, the fiber model and simulation method presented in Ref. 1 is briefly reviewed. Inertia and hydrodynamic interactions between beads are neglected, but hydrodynamic interactions with the bounding surfaces are included in certain cases. Simulation results are presented in Sec. III. In Sec. III A, we show that the fiber model accurately reproduces numerous features of Jeffery's analysis for stiff fibers. In Sec. III B, we illustrate that this fiber model can accurately simulate the ''pole-vaulting'' motion of stiff fibers near rigid bounding surfaces, but that the results depend sensitively on the short-range interactions between the fiber and the surface. In Sec. III C, we describe simulation results for the motion of isolated flexible fibers in shear flows. In contrast to Jeffery's analysis for rigid fibers, flexible fiber orbits drift, and the orbit period depends on the fiber orientation. The configurational dynamics of these model fibers closely follow those observed experimentally by Arlov *et al.*[9] Finally, the main conclusions from this work are summarized in Sec. IV.

II. MODEL AND SIMULATION METHOD

A. Fiber model connectivity

The fiber is composed of N rigid bodies connected by N hinges as illustrated in Fig. 2. Arbitrarily shaped rigid bodies can be employed in the general method presented here, but for simplicity, we restrict attention to spherical

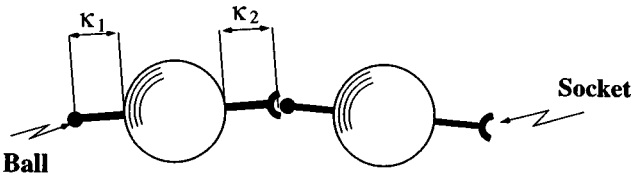

FIG. 2. A portion of a model fiber, illustrating the geometry of the fiber subunits. A massless rod with a ball at one end and a socket at the other passes through the center of mass of a sphere. The rod is positioned so that the ball and socket protrude distances of κ_1 and κ_2 from the sphere surface, respectively.

beads of diameter σ (radius a). $N-1$ of the hinges are real, with one fictitious hinge connecting the fiber to a reference frame. The degrees of freedom in each hinge may be varied between 0 and 6; for the $N-1$ real hinges, we use ball and socket joints, each having 3 rotational degrees of freedom and thus limiting our model to inextensible fibers. The fictitious hinge coupling the fiber to the reference frame possesses 6 degrees of freedom allowing the fiber to translate and rotate freely.

The fiber connectivity and kinematics, described by the methods discussed by Wittenburg[15], have been presented in detail in Ref. 1. Here we outline the features pertinent to this paper. Bodies are referred to with greek indices $(\nu,\eta,\kappa,\lambda,\ldots=1,\ldots,N)$ and hinges are referred to with latin indices $(a,b,c,\ldots=1,\ldots,N)$. The interconnected fiber model is described by sets of vertices (the rigid bodies) and directed arcs (the hinges). Arc a emanates from vertex $i^+(a)$, and is directed toward vertex $i^-(a)$. For the linear collection of beads considered here, these integer functions are $i^+(a)=a-1$, and $i^-(a)=a$. Body 1, termed the *base*, is connected to the reference frame through the fictitious hinge; body N is termed the *tip*. The integer functions $i^+(a)$ and $i^-(a)$ give the indices of the body inboard (towards the base) and outboard (away from the base) of the hinge, respectively.

The elements of the connectivity matrix $\mathbf{S}$ and its inverse, the topology matrix $\mathbf{T}$, are defined by

$$S_{\nu a}=\begin{cases} -1 & \text{if (a) is the inboard hinge on body } (\nu) \\ +1 & \text{if (a) is the outboard hinge on body } (\nu) \\ 0 & \text{if hinge (a) is not on body } (\nu) \end{cases},$$

$$T_{a\nu}=\begin{cases} -1 & \text{if body } (\nu) \text{ lies outboard of hinge (a)} \\ 0 & \text{otherwise} \end{cases}. \quad (7)$$

The two matrices are related through the identities

$$\mathbf{T}\cdot\mathbf{S}=\mathbf{S}\cdot\mathbf{T}=\boldsymbol{\delta}, \quad (8)$$

where $\boldsymbol{\delta}$ is the $N\times N$ identity matrix.

B. Kinematics

For convenience, the fiber kinematics are described in terms of three sets of body-fixed vectors. The first set of vectors, $\mathbf{c}_{\nu a}$, connect the center of mass of body ν to hinge

a, if hinge a is attached to body ν; otherwise $\mathbf{c}_{\nu a}$ is zero. The connectivity of two contiguous bodies is described by the vector equation

$$[\mathbf{r}_{i^-(a)}+\boldsymbol{c}_{i^+(a)a}]-[\mathbf{r}_{i^+(a)}+\boldsymbol{c}_{i^-(a)a}]=\mathbf{0}, \tag{9}$$

where $\mathbf{r}_\nu$ is the position of the center of mass of body ν. Using the connectivity matrix $\mathbf{S}$, these constraint equations may be combined into a single matrix equation,

$$\mathbf{S}^\dagger\cdot\underline{\mathbf{r}}+\mathbf{C}^\dagger\cdot\underline{\mathbf{1}}_N=\mathbf{0}, \tag{10}$$

where $\underline{\mathbf{r}}=[\mathbf{r}_1\cdots\mathbf{r}_N]^\dagger$, $\mathbf{1}_N$ is an $N\times 1$ matrix of ones, and $\mathbf{C}$ is an $N\times N$ matrix with vector components $\mathbf{C}_{\nu a}=S_{\nu a}\mathbf{c}_{\nu a}$ (the superscript † denotes the transpose). Premultiplying Eq. (10) with $\mathbf{T}^\dagger$ and using Eq. (8), the bead positions may be expressed as

$$\underline{\mathbf{r}}=-\{\mathbf{C}\cdot\mathbf{T}\}^\dagger\cdot\underline{\mathbf{1}}_N \text{ or } \mathbf{r}_\nu=-\sum_{\eta=1}^{N}\mathbf{d}_{\eta\nu}, \tag{11}$$

where we have introduced a second set of body-fixed vectors $\mathbf{d}_{\eta\nu}=\{\mathbf{C}\cdot\mathbf{T}\}_{\eta\nu}$. There are $2(N-1)$ distinct body-fixed vectors $\mathbf{d}_{\eta\nu}$, which have a simple interpretation: if $\eta=\nu$, $\mathbf{d}_{\eta\nu}$ is the vector on body η directed from its center of mass to the inboard hinge; if body ν lies outboard of body η, then $\mathbf{d}_{\eta\nu}$ is the vector directed from the outboard hinge to the inboard hinge of body η; otherwise it is zero.

It is convenient to change the frame of reference in Eq. (11) from the reference frame to the fiber center of mass using

$$\mathbf{r}_\nu=\mathbf{R}_\nu+\mathbf{r}_{cm}, \tag{12}$$

where $\mathbf{R}_\nu$ is the position of bead ν relative to the fiber center of mass, $\mathbf{r}_{cm}$. Substituting Eq.(12) into Eq.(11) and premultiplying by the $N\times N$ matrix $\mathbf{m}$ ($m_{\nu\eta}=\delta_{\nu\eta}-m_\nu/m_f$, where m_ν and m_f are the masses of bead ν and the fiber, respectively), the bead positions relative to the center of mass are

$$\underline{\mathbf{R}}=-\{\mathbf{C}\cdot\mathbf{T}\cdot\mathbf{m}\}^\dagger\cdot\underline{\mathbf{1}}_N \text{ or } \mathbf{R}_\nu=\sum_{\eta=1}^{N}\mathbf{b}_{\eta\nu}, \tag{13}$$

where the third set of body-fixed vectors are $\mathbf{b}_{\eta\nu}=-\{\mathbf{C}\cdot\mathbf{T}\cdot\mathbf{m}\}_{\eta\nu}$. Substituting Eq. (13) into Eq. (12), the absolute particle positions are expressed

$$\mathbf{r}_\nu=\sum_{\eta=1}^{N}\mathbf{b}_{\eta\nu}+\mathbf{r}_{cm}. \tag{14}$$

The translational velocity of body ν is

$$\dot{\mathbf{r}}_\nu=\sum_{\eta=1}^{N}\boldsymbol{\omega}_\eta\times\mathbf{b}_{\eta\nu}+\dot{\mathbf{r}}_{cm}, \tag{15}$$

where $\boldsymbol{\omega}_\eta$ is the absolute angular velocity of body η. The absolute angular velocity of body η is related to the relative angular velocities of the other bodies through the matrix $\mathbf{T}$,

$$\boldsymbol{\omega}_\eta=-\sum_{a=1}^{N}T_{a\eta}\boldsymbol{\Omega}_a, \tag{16}$$

where $\boldsymbol{\Omega}_a$ is the angular velocity of the body outboard of hinge a relative to the body inboard of hinge a.

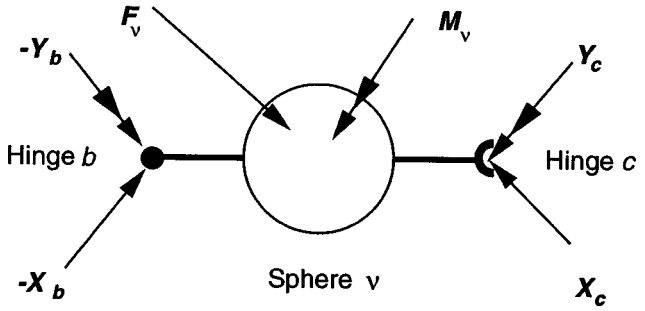

FIG. 3. Free body diagram of subunit ν. Constraint forces $-\mathbf{X}_b$ and $\mathbf{X}_c$, and hinge torques $-\mathbf{Y}_b$ and $\mathbf{Y}_c$ act at the ball and socket joints. The resultant external force $\mathbf{F}_\nu$ and torque $\mathbf{M}_\nu$ act through the center of mass of the sphere.

The transformation between the reference frames of two contiguous bodies connected by hinge a is given by $\mathbf{e}_{i^+(a)}=\mathbf{G}_a\cdot\mathbf{e}_{i^-(a)}$, where $\mathbf{e}_{i^+(a)}$ and $\mathbf{e}_{i^-(a)}$ are the matrices whose columns are the Cartesian base vectors of the body-fixed reference frames of the two bodies connected by hinge a. The orthogonal transformation matrix $\mathbf{G}_a$ is given in terms of Euler parameters in Refs. 1 and 15.

C. Dynamics

The free body diagram for bead ν is shown in Fig. 3. $\mathbf{F}_\nu$ is the resultant external force acting through the center of mass, $\mathbf{M}_\nu$ is the resultant external torque, $\mathbf{X}_b$ and $\mathbf{X}_c$ are the internal constraint forces in joints b and c respectively, and $\mathbf{Y}_b$ and $\mathbf{Y}_c$ are the resultant internal torques in the corresponding joints.

1. Linear momentum balance

Newton's second law for bead ν takes the form

$$m_\nu\ddot{\mathbf{r}}_\nu=\mathbf{F}_\nu+\sum_{a=1}^{N}S_{\nu a}\mathbf{X}_a, \tag{17}$$

where $\ddot{\mathbf{r}}_\nu$ is the translational acceleration of bead ν. The resultant external force is a combination of hydrodynamic forces $\mathbf{F}_\nu^{(h)}$, and interparticle forces $\mathbf{F}_\nu^{(p)}$. Body forces may also be included, but are ignored in this investigation.

Neglecting hydrodynamic interactions between different beads, as well as fluid inertia, the hydrodynamic force on bead ν suspended in a Newtonian fluid may be expressed

$$\mathbf{F}_\nu^{(h)}=\boldsymbol{\zeta}_\nu^t\cdot[\mathbf{U}_\nu^\infty-\dot{\mathbf{r}}_\nu], \tag{18}$$

where $\dot{\mathbf{r}}_\nu$ and $\mathbf{U}_\nu^\infty$ are the translational velocity of bead ν and the ambient fluid velocity at the center of mass of bead ν. The hydrodynamic translation resistance tensor $\boldsymbol{\zeta}_\nu^t$, described in more detail below, may be anisotropic and position dependent.

The interparticle force $\mathbf{F}_\nu^{(p)}$ describes any intrafiber interactions such as colloidal forces and short-range repulsion (i.e., excluded volume), as well as repulsion from system boundaries (only single fibers are considered in this paper). The intrafiber force is represented here by a short-range function of the form

$$\mathbf{F}_{\nu\mu}^{(p,f)} = -F_0 \exp\left(-10\frac{|\mathbf{r}_\nu - \mathbf{r}_\mu|}{\sigma}\right)\mathbf{e}_{\nu\mu}, \tag{19}$$

where F_0 is the magnitude of the short-range repulsive force, and $\mathbf{e}_{\nu\mu} = (\mathbf{r}_\nu - \mathbf{r}_\mu)/|\mathbf{r}_\nu - \mathbf{r}_\mu|$ is the unit vector along the line joining the centers of beads ν and μ. The excluded volume interaction with the system boundaries is expressed similarly,

$$\mathbf{F}_{\nu}^{(p,b)} = -F_0 \exp\left(-10\frac{(h_\nu - a) - \delta_{shift}}{\sigma}\right)\mathbf{n}_b, \tag{20}$$

where h_ν is the normal distance between the center of bead ν and the bounding surface, δ_{shift} is a shift factor for the repulsive force (discussed below), and $\mathbf{n}_b$ is the surface normal of the boundary with which bead ν is interacting.

Inserting Eq. (15) into Eq. (18) and substituting into Eq. (17), the motion of the fiber center of mass is obtained by summing the resulting set of translational equations of motion for each bead. Neglecting inertia,

$$\dot{\mathbf{r}}_{cm} = -\boldsymbol{\mu}\cdot\sum_{\nu=1}^{N}\sum_{\mu=1}^{N}\boldsymbol{\zeta}_\nu^t\cdot[\boldsymbol{\omega}_\mu\times\mathbf{b}_{\mu\nu}] + \boldsymbol{\mu}\cdot\sum_{\nu=1}^{N}(\boldsymbol{\zeta}_\nu^t\cdot\mathbf{U}_\nu^\infty + \mathbf{F}_\nu^{(p)}], \tag{21}$$

where $\boldsymbol{\mu} = \{\Sigma_{\eta=1}^{N}\boldsymbol{\zeta}_\eta^t\}^{-1}$. As the translational resistance tensors and the ambient fluid velocity profile will be specified, Eqs. (15) and (21) express the bead and center of mass translational velocities, respectively, in terms of the bead positions and absolute angular velocities. The angular velocities are determined by the angular momentum balance described below.

2. Angular momentum balance

The angular momentum balance for body ν is

$$\dot{\mathbf{H}}_\nu = \mathbf{M}_\nu + \sum_{a=1}^{N} S_{\nu a}[\mathbf{c}_{\nu a}\times\mathbf{X}_a + \mathbf{Y}_a], \tag{22}$$

where $\dot{\mathbf{H}}_\nu$ is the time rate of change of angular momentum of bead ν. The resultant external torque $\mathbf{M}_\nu$ is a combination of the hydrodynamic torque $\mathbf{M}_\nu^{(h)}$, and torques produced by external moments or interparticle forces not acting through the bead center of mass, $\mathbf{M}_\nu^{(p)}$.

If inertia is again neglected, the hydrodynamic torque acting on bead ν in a Newtonian fluid with vorticity $\boldsymbol{\Omega}_\nu^\infty$ at the bead center of mass may be represented by

$$\mathbf{M}_\nu^{(h)} = \boldsymbol{\zeta}_\nu^r\cdot(\boldsymbol{\Omega}_\nu^\infty - \boldsymbol{\omega}_\nu). \tag{23}$$

The hydrodynamic rotation resistance tensor $\boldsymbol{\zeta}_\nu^r$ will be described below.

Fiber bending and twisting elasticity is incorporated into the model through resultant internal torques in the joints, $\mathbf{Y}_a$ $(a = 2, \ldots, N)$. Bending and twisting torques are defined independently and superposed. The bending torque, $\mathbf{Y}_a^{(B)}$, defined in terms of the angle θ_a between vectors $\mathbf{c}_{i^+(a)a}$ and $-\mathbf{c}_{i^-(a)a}$, is assumed to be proportional to the difference between this angle and its equilibrium value

$$\mathbf{Y}_a^{(B)} = -k^{(B)}(\theta_a - \theta_a^{eq})\mathbf{n}_{pb}, \tag{24}$$

where $\mathbf{n}_{pb} = (\mathbf{c}_{i^-(a)a}\times\mathbf{c}_{i^+(a)a})/(|\mathbf{c}_{i^-(a)a}\times\mathbf{c}_{i^+(a)a}|)$ is the unit vector normal to the plane of bending, and θ_a is given by $\cos\theta_a = -(\mathbf{c}_{i^-(a)a}\cdot\mathbf{c}_{i^+(a)a})/(|\mathbf{c}_{i^-(a)a}||\mathbf{c}_{i^+(a)a}|)$. The bending constant $k^{(B)}$ describes the bending stiffness of the fiber, and is related to the bending stiffness of an equivalent elastic cylinder (Young's modulus E, moment of inertia I, and radius a) for small deformations via $k^{(B)} = (EI)/(2a)$. The twisting torque $\mathbf{Y}_a^{(T)}$ is defined in terms of the twist angle ϕ_a between two contiguous bodies about the axis defined by $\mathbf{c}_{i^+(a)a}$, and is again assumed to be proportional to the difference between ϕ_a and its equilibrium value ϕ_a^{eq},

$$\mathbf{Y}_a^{(T)} = -k^T(\phi_a - \phi_a^{eq})\mathbf{n}_{pt}, \tag{25}$$

where $\mathbf{n}_{pt} = \mathbf{c}_{i^+(a)a}/|\mathbf{c}_{i^+(a)a}|$. In order to calculate the twist angle, the body-fixed unit vector $\mathbf{u}_{i^+(a)a}$ directed along the x axis of the local coordinate system attached to body $i^+(a)$ is employed. The angle ϕ_a is given by $\cos\phi_a = (\mathbf{u}'_{i^-(a)a}\cdot\mathbf{u}_{i^+(a)a})/(|\mathbf{u}'_{i^-(a)a}||\mathbf{u}_{i^+(a)a}|)$, where $\mathbf{u}'_{i^-(a)a} := \mathbf{u}_{i^-(a)a} - (\mathbf{u}_{i^-(a)a}\cdot\mathbf{n}_{pt})\mathbf{n}_{pt}$. The torsional rigidity of the fiber $k^{(T)}$ is related to the torsional rigidity of an equivalent elastic cylinder (shear modulus G, polar moment J) for small deformations via $k^{(T)} = (GJ)/(2a)$. The above relations for the hinge torques are assumed to hold for all deflections. Nonuniform fiber properties may be modeled by allowing $k^{(B)}$ and $k^{(T)}$ to vary along the fiber. Permanent deformations may be modeled by altering θ_a^{eq} and ϕ_a^{eq}. For a straight, nontwisted fiber, $\theta_a^{eq} = 0$ and $\phi_a^{eq} = 0$.

Neglecting bead inertia, the angular momentum balance reduces to

$$\mathbf{M}_\nu^{(h)} + \mathbf{M}_\nu^{(p)} + \sum_{a=1}^{N} S_{\nu a}(\mathbf{c}_{\nu a}\times\mathbf{X}_a + \mathbf{Y}_a) = \mathbf{0}. \tag{26}$$

The constraint forces appearing in Eq. (26) are eliminated by rewriting the N vector equations in Eq. (17) in matrix form (neglecting inertia), solving for the constraint forces, and substituting the result into Eq. (26). Further substituting Eq. (18) for the hydrodynamic force, and Eq. (15) for the bead translational velocities, yields

$$\sum_{\eta=1}^{N}\mathbf{Z}_{\nu\eta}\cdot\boldsymbol{\omega}_\eta = \mathbf{t}_\nu, \tag{27}$$

where

$$\mathbf{Z}_{\nu\eta} := \delta_{\nu\eta}\boldsymbol{\zeta}_\nu^r + \sum_{\kappa=1}^{N}\tilde{\mathbf{d}}_{\nu\kappa}\cdot\boldsymbol{\zeta}_\kappa^t\cdot\tilde{\mathbf{b}}_{\eta\kappa} - \sum_{\kappa=1}^{N}\sum_{\lambda=1}^{N}\tilde{\mathbf{d}}_{\nu\kappa}\cdot\boldsymbol{\zeta}_\kappa^t\cdot\boldsymbol{\mu}\cdot\boldsymbol{\zeta}_\lambda^t\cdot\tilde{\mathbf{b}}_{\eta\lambda}, \tag{28}$$

$$\mathbf{t}_\nu := \mathbf{M}_\nu^{(p)} + \sum_{a=1}^{N} S_{\nu a}\mathbf{Y}_a + \boldsymbol{\zeta}_\nu^{r}\boldsymbol{\Omega}_\nu^{\infty} - \sum_{\kappa=1}^{N} \mathbf{d}_{\nu\kappa}\times(\boldsymbol{\zeta}_\kappa^{t}\cdot\mathbf{U}_\kappa^{\infty} + \mathbf{F}_\kappa^{(p)}) + \sum_{\kappa=1}^{N} \mathbf{d}_{\nu\kappa}\times\left(\boldsymbol{\zeta}_\kappa^{t}\cdot\boldsymbol{\mu}\cdot\sum_{\lambda=1}^{N}\boldsymbol{\zeta}_\lambda^{t}\cdot\mathbf{U}_\lambda^{\infty} + \mathbf{F}_\lambda^{(p)}\right), \tag{29}$$

where matrices $\tilde{\mathbf{a}}$ are defined $\tilde{a}_{ij} = -\epsilon_{ijk}a_k$, where ϵ_{ijk} is the permutation operator. Eq. (27) represents a coupled set of linear vector equations. Since $\mathbf{Z}_{\nu\eta}$ and $\mathbf{t}_\nu$ are functions of only the bead positions and orientations, Eq. (27) can be solved numerically for the absolute bead angular velocities.

The dynamic simulation algorithm consists of using the solution for the absolute angular velocities to update the bead positions and orientations. Using the relative angular velocities $\boldsymbol{\Omega}_\nu$ determined from Eq. (16), the time derivatives of the Euler parameters may be computed via

$$\begin{bmatrix} \dot{q}_{1\nu} \\ \dot{q}_{2\nu} \\ \dot{q}_{3\nu} \\ \dot{q}_{4\nu} \end{bmatrix} = \frac{1}{2}\begin{bmatrix} 0 & -\Omega_\nu^x & -\Omega_\nu^y & -\Omega_\nu^z \\ \Omega_\nu^x & 0 & \Omega_\nu^z & -\Omega_\nu^y \\ \Omega_\nu^y & -\Omega_\nu^z & 0 & \Omega_\nu^x \\ \Omega_\nu^z & \Omega_\nu^y & -\Omega_\nu^x & 0 \end{bmatrix}\cdot\begin{bmatrix} q_{1\nu} \\ q_{2\nu} \\ q_{3\nu} \\ q_{4\nu} \end{bmatrix}. \tag{30}$$

The Euler parameters give the orientation of body ν relative to body $\nu-1$, and thus the relative angular velocities must be transformed to the local coordinate system of body ν. The bead orientations are updated via numerical (Euler) integration of Eq. (29). The Euler parameters should be periodically normalized during the simulation to prevent propagation of computer round-off error. The fiber center of mass is updated by numerical (Euler) integration of Eq. (21), and the bead positions are updated directly through their relationships with the bead orientations,

$$\mathbf{r}_\nu^{new} = \mathbf{r}_{cm}^{new} + \sum_{\mu=1}^{N} \mathbf{b}_{\nu\mu}. \tag{31}$$

Dimensionless variables are obtained by choosing time, length and force scales. In this work, the length scale is the bead diameter, $\sigma = 2a$, the time scale is the inverse of the characteristic shear rate, $\dot{\gamma}^{-1}$, and the force scale is the characteristic hydrodynamic force, $\pi\sigma^2\eta_0\dot{\gamma}$ (η_0 is the continuous phase viscosity). Dimensionless variables will be indicated with a superscripted asterisk.

D. Hydrodynamic resistance tensors

In the limit of zero particle Reynolds number, $\mathrm{Re} = \rho a^2\dot{\gamma}/\eta_0$, the hydrodynamic resistance tensors $\boldsymbol{\zeta}_\eta^{t}$ and $\boldsymbol{\zeta}_\eta^{r}$ are functions of all the bead positions as well as the positions of the bounding surfaces. For isolated spheres, these tensors are

$$\boldsymbol{\zeta}_\eta^{t} = 6\pi\eta_0 a\,\boldsymbol{\delta}, \tag{32}$$

$$\boldsymbol{\zeta}_\eta^{r} = 8\pi\eta_0 a^3\boldsymbol{\delta}. \tag{33}$$

At finite separations between the beads and between the beads and the walls, these expressions are modified by hydrodynamic interactions[16–18].

In this study, we ignore hydrodynamic interactions between beads, but in some cases (discussed below) approximate the hydrodynamic interaction between each bead and a bounding surface. We employ asymptotic far-field or near-field forms for the interactions[16–18], depending upon the relative separation between the bead and the wall. Choosing the y axis normal to the wall, the resistance tensors are expressed

$$\boldsymbol{\zeta}_\eta^{t} = 6\pi\eta_s a\begin{bmatrix} \zeta_{\parallel\eta}^{t}(\epsilon_{\eta b}) & 0 & 0 \\ 0 & \zeta_{\perp\eta}^{t}(\epsilon_{\eta b}) & 0 \\ 0 & 0 & \zeta_{\parallel\eta}^{t}(\epsilon_{\eta b}) \end{bmatrix}, \tag{34}$$

$$\boldsymbol{\zeta}_\eta^{r} = 8\pi\eta_s a^3\begin{bmatrix} \zeta_{\parallel\eta}^{r}(\epsilon_{\eta b}) & 0 & 0 \\ 0 & \zeta_{\perp\eta}^{r}(\epsilon_{\eta b}) & 0 \\ 0 & 0 & \zeta_{\parallel\eta}^{r}(\epsilon_{\eta b}) \end{bmatrix} \tag{35}$$

with the scalar functions $\zeta_{\parallel\eta}^{t}$, $\zeta_{\perp\eta}^{t}$, $\zeta_{\parallel\eta}^{r}$ and $\zeta_{\perp\eta}^{r}$ given by

$$\zeta_{\parallel\eta}^{t}(\epsilon_{\eta b}) = \begin{cases} -\dfrac{8}{15}\ln(\epsilon_{\eta b}) + 0.9588 & \epsilon_{\eta b} < \epsilon_{\parallel}^{t} \\ \left(1 - \dfrac{9}{16}\dfrac{1}{1+\epsilon_{\eta b}} + \dfrac{1}{8}\dfrac{1}{(1+\epsilon_{\eta b})^3} - \dfrac{45}{256}\dfrac{1}{(1+\epsilon_{\eta b})^4} - \dfrac{1}{16}\dfrac{1}{(1+\epsilon_{\eta b})^5}\right)^{-1} & \epsilon_{\eta b} > \epsilon_{\parallel}^{t} \end{cases}$$

$$\zeta_{\perp\eta}^{t}(\epsilon_{\eta b}) = \begin{cases} \dfrac{1}{\epsilon_{\eta b}} + \dfrac{1}{5}\ln(\epsilon_{\eta b}) + 0.971264 & \epsilon_{\eta b} < \epsilon_{\perp}^{t} \\ \left(1 - \dfrac{9}{8}\dfrac{1}{(1+\epsilon_{\eta b})} + \dfrac{1}{2}\dfrac{1}{(1+\epsilon_{\eta b})^3}\right)^{-1} & \epsilon_{\eta b} > \epsilon_{\perp}^{t} \end{cases}$$

$$\zeta_{\parallel \epsilon^r}(\epsilon_{\epsilon b}) = \begin{cases} -\frac{2}{5}\ln(\epsilon_{\eta b}) + 0.3817 & \epsilon_{\eta b} < \epsilon_{\parallel}^{r} \\ 1 + \frac{5}{16}\frac{1}{(1+\epsilon_{\eta b})^3} & \epsilon_{\eta b} > \epsilon_{\parallel}^{r}, \end{cases}$$

$$\zeta_{\perp\,\eta}^{r}(\epsilon_{\eta b}) = 1 \,\forall\, \epsilon_{\eta b}. \tag{36}$$

Here, $\epsilon_{\eta b} = (h_\nu - a)/a$, where h_ν is the distance between the center of sphere ν and the wall. The crossover separations $\epsilon_{\parallel}^{t}$, $\epsilon_{\perp}^{t}$ and $\epsilon_{\parallel}^{r}$ are 0.941374, 0.034382, and 0.122728, respectively.

E. Flow fields

Two different flow fields are investigated in this paper: a simple shear flow driven by a moving upper plate,

$$\mathbf{U}^{\infty} = \left[\dot{\gamma} H \left(\tfrac{1}{2} + \frac{y}{H} \right), 0, 0 \right]$$

and a parabolic pressure-driven shear flow,

$$\mathbf{U}^{\infty} = \left[\dot{\gamma} H \left(1 - \left(1 - \frac{y}{H} \right)^2 \right), 0, 0 \right].$$

Unbounded flows are implemented by neglecting all interactions with the bounding surfaces [Eqs. (35)], and the dynamics of fibers close to a wall are implemented by employing interactions with the closest wall only [located at $y = -(1/2)H$]. The distance between the bounding surfaces is always larger than the fiber contour length.

III. RESULTS

A. Stiff fibers in unbounded flow

Simulations in unbounded flows were performed for fibers composed of N spheres with $N \in \{4, \ldots, 20\}$, $F_0^* = 1.0$, and for the combinations of the model parameters $(\kappa_1^*, \kappa_2^*) = \{(0.1,0),(0.1,0.1)\}$. The bending and twisting stiffnesses were $k^{(B)*} = 2500$ and $k^{(T)*}/k^{(B)*} = 2/3$, ensuring that the fibers remained rigid (i.e., the end-to-end distance changed by less than 0.2% during an orbit). Simulations were performed for a series of orbit constants $C \in \{0.05, 0.1, 0.2, 0.5, 2, 10, \infty\}$, and the motion was monitored for four full periods, with selected runs of up to 20 periods. No visible drift could be observed when plotting the orbits traced out by the end-to-end vector, in agreement with predictions[2,6,7].

The dimensionless period $T\dot{\gamma}$ is plotted as a function of aspect ratio $a_r = 1 + (N-1)^*(1 + \kappa_1^* + \kappa_2^*)$ in Fig. 4, along with Jeffery's predictions and experimental data reported by Trevelyan and Mason[3] for bundled glass fiber cylinders. The period is independent of orbit constant, and identical for simple shear and parabolic velocity profiles, as predicted. No visible drift in the period or orbit constant was observed during the simulations. We will return to this issue in Sec. III C, where the drift is investigated as a function of bending stiffness.

The simulated periods in Fig. 4 increase with aspect ratio in a manner qualitatively similar to Jeffrey's predictions and the experimental data. Quantitative differences arise from two different features. First, different shapes (e.g., prolate spheroids, cylinders, etc.) produce different orbit periods, and thus chains of osculating bodies should not have the same period as a single prolate spheroid of the same aspect ratio. Using an approximate analysis, Burgers[19] found that periods of long, blunt-ended cylinders were about 26% smaller than those of prolate spheroids of the same aspect ratio. Using boundary integral methods to accurately determine the rotational motion of rigid, elongated bodies, Ingber and Mondy[20] found that the rotational period of a blunt-ended cylindrical rod was about 20% less than that of a prolate spheroid of the same aspect ratio. Second, our simulations neglect hydrodynamic interactions between the beads. The relative contributions of these two features in the deviation of the simulated periods from those of prolate spheroids is not known.

The equivalent aspect ratio of a fiber, a_{r_e}, is found by

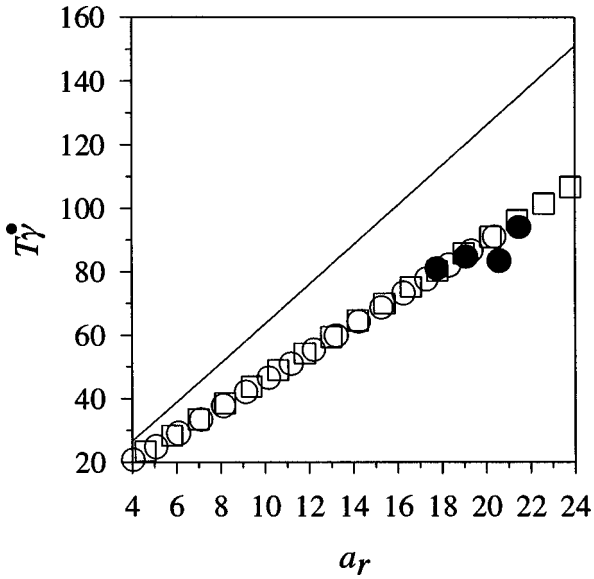

FIG. 4. The dimensionless orbit period, $T\dot{\gamma}$, as a function of aspect ratio a_r. Open squares—simulation results with $\kappa_1 = \kappa_2 = 0.1$; open circles—simulation results using $\kappa_1 = 0.1$ and $\kappa_2 = 0$; filled circles—experimental data for rigid cylinders [3]; solid curve—Jeffery's analysis for a prolate spheroid. Results are identical for simple and parabolic shear flows.

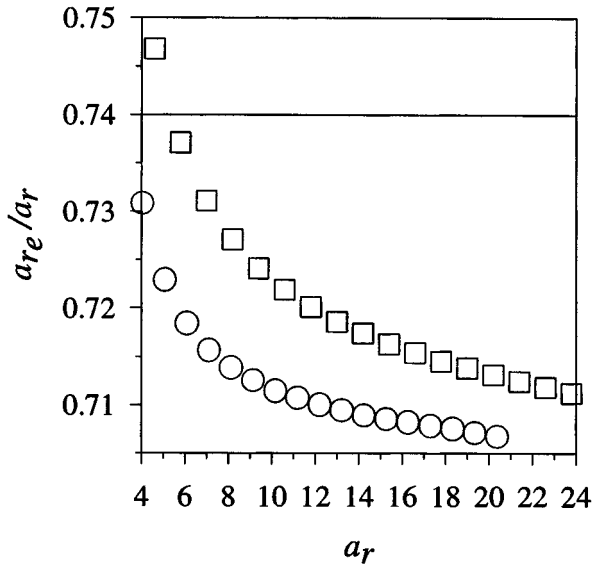

FIG. 5. Ratio of equivalent to actual aspect ratio as a function of actual aspect ratio. Squares—fiber model using $\kappa_1=\kappa_2=0.1$; circles—$\kappa_1=0.1$ and $\kappa_2=0$; solid line—approximate value obtained by Burgers (see Ref. 19) for rigid cylinders. Results are identical for simple and parabolic shear flows.

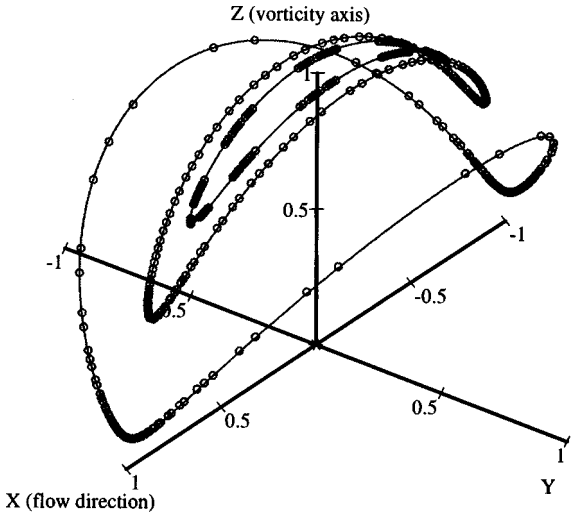

FIG. 6. Comparison between simulated orbits (open circles) and Jeffery's predictions (solid curves). Three orbit constants are shown: $C=0.05, 0.1$, and 0.5. The nonuniform spacing of the simulated values is an artifact of the periodic sampling of the fiber configurations. Data shown are from the fourth full period after starting the simulation. Results are identical for simple and parabolic shear flows.

substituting the experimental or simulated value for $T\dot{\gamma}$ into Eq. (3). The ratio a_{r_e}/a_r is commonly reported, and a value of $\simeq 0.74$ is expected for long cylinders[19]. Experiments with real fibers[3,5] show that a_{r_e}/a_r decreases with increasing a_r. This trend is also observed in our simulation results, illustrated in Fig. 5, where a_{r_e}/a_r is plotted as a function of a_r for $\{\kappa_1^*,\kappa_2^*\}=\{0.1,0.1\}$ and $\{0.1,0\}$. The equivalent aspect ratio is identical for simple shear and parabolic velocity profiles, but depends on the details of the fiber model (e.g., the values of κ_1^* and κ_2^*).

Simulated fiber orbits are again compared to Jeffery's predictions in Fig. 6, where the trajectories of the normalized end-to-end vectors (open circles) are plotted for $C=0.05$, 0.1, and 0.5. The solid curves are Jeffery's predictions for an aspect ratio equal to the equivalent aspect ratio of the simulated fiber. The agreement is excellent, implying that hydrodynamic interactions influence the value of the equivalent aspect ratio, but not the trajectories.

The comparison between the simulation results and Jeffery's analysis for stiff fibers with $N=15$ and $\kappa_1^*,\kappa_2^*=0.1$ is summarized in Table I for a series of orbit constants.

B. Stiff fibers near a bounding surface

Stover and Cohen[21] investigated the behavior of single rigid fibers near a plane wall in a pressure-driven Hele–Shaw flow, in both Newtonian and non-Newtonian liquids. Fibers whose elliptic orbits would penetrate the wall performed a ''pole-vault,'' with the fiber center of mass translating irreversibly to approximately one half of a fiber length away from the wall (for $C\approx\infty$). The orbit period for fibers close to the wall increased, which was reported as an apparent increase in a_{r_e}/a_r. Examination of $\dot{\phi}$ and $\dot{\theta}$ suggested that the slowdown was uniform in time.

Since such irreversible fiber dynamics arise from nonhydrodynamic forces, simulations in simple shear flow $(H/\sigma=50)$ with three different treatments of the fiber–wall interaction were performed. First, the wall interaction included only a short-range repulsive force [Eq. (20) with $\delta_{shift}=0$], neglecting hydrodynamic interactions between the beads and the wall. Fiber parameters were $N=15$, $k^{(B)}*=2500$, $k^{(T)}*/k^{(B)}*=2/3$, $\kappa_1=0.0$, $\kappa_2=0.1$, and $F_0^*=1.0$. This produces pole-vaulting, but no period slowdown. Sequences of fiber snaphots during pole-vaulting simulations are illustrated in Fig. 7. We note that when the fiber end is close to the wall, the fiber bends significantly more than in unbounded shear flow. This is due to a large compressive axial force arising from the repulsion from the wall.

In the second treatment, hydrodynamic interactions between the beads and the wall were added to this repulsive force. Hydrodynamic interactions between the beads were not included. Using this approach, the fiber does not pole-vault irreversibly as observed experimentally [Fig. 7(b)]. The fiber bends even more than in the first treatment, due to a larger compressive axial force resulting from hydrodynamic lubrication at the wall. As the fiber completes a rotation of

TABLE I. Comparison between simulations and predictions from Jeffrey's analysis. Tabulated are the ratios of various simulated to analytical quantities (for the same equivalent aspect ratio).

C	n	λ_{xz}	λ_{yz}	a_{xy}	b_{xy}
∞	1.00	1.00	1.00	1.00	1.00
2	1.00	1.00	1.00	1.00	1.00
0.5	1.00	1.00	1.00	1.00	1.00
0.1	1.00	1.00	1.00	1.00	1.00
0.05	1.00	1.00	1.00	1.00	1.00

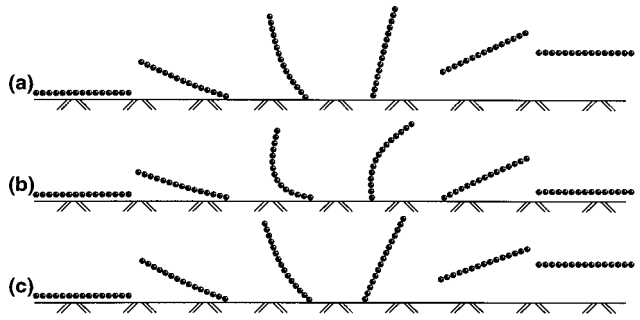

FIG. 7. Pole-vault of fibers near a wall in simple shear flow ($C=\infty$, $k^{(B)*}=2500$, $H/\sigma=50$). (a) No hydrodynamic interactions between fiber and wall, no shift in excluded volume. (b) Hydrodynamic interactions included, no shift in excluded volume. (c) Hydrodynamic interactions included, $\delta_{shift}=0.05\sigma$. In (c) the pole-vault is essentially complete during the first half period, but the fiber center of mass oscillates for several periods. This is expected since the fiber continues to interact hydrodynamically with the wall. Peak oscillations are pronounced for $\phi=0°$ and $\phi=180°$, indicating that lubrication is the dominant factor. If δ_{shift} is increased, the oscillations and the fiber curvature are reduced. Oscillations are likely too small (amplitude $\approx 0.2\sigma$) to be seen experimentally.

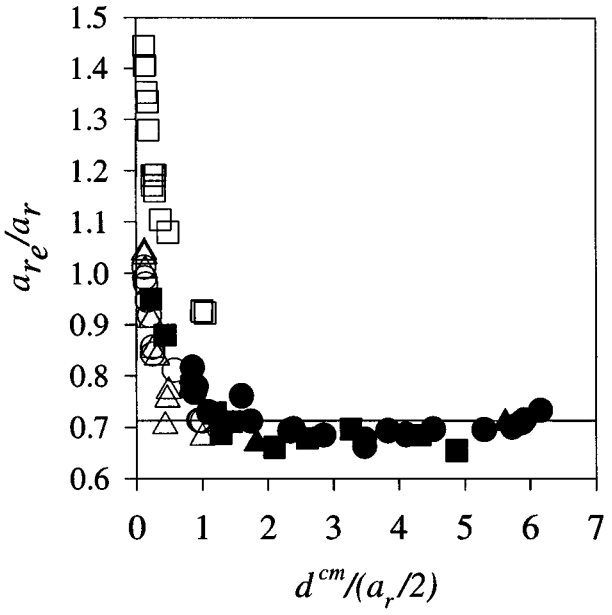

FIG. 8. a_{r_e}/a_r as a function of $d^{cm}/(a_r/2)$, where d^{cm} is the separation between the fiber center of mass and the bounding surface. Simulation results are for $C^0=\{0.05,0.1,0.5,\infty\}$ and $d^{cm,0}=\{\ell,2\ell\}$, where ℓ is the orbit-dependent separation at which a fiber will just contact the surface. Open circles—simple shear flow, $k^{(B)*}=30$; open triangles—simple shear flow, $k^{(B)*}=2500$; open squares—parabolic shear flow, $k^{(B)*}=2500$; filled circles/squares—experimental data, small/large initial orbit constants (see Ref. 21); filled triangles—experimental data (see Ref. 5); solid line—simulated value obtained in unbounded flow.

180°, it does not translate to half of a fiber length away from the wall, but rather continues to rotate toward the wall. This suggests that the relative contribution of our approximation for hydrodynamic interaction to the fiber motion is too large.

Bossis and Brady[22] observed that the character of short-range repulsive forces can have a significant influence on the structure and dynamics of suspensions of spherical particles. In particular, for sufficiently short-range repulsive forces, the suspension structure was controlled by lubrication forces; when the range of the repulsive force was increased sufficiently, the structure changed, apparently by attenuating the lubrication forces. To further investigate the influence of the short-range repulsive force on pole-vaulting, a third treatment was employed where the short-range repulsive force was altered by varying the value of δ_{shift} in Eq. (20) (and equivalent to the second treatment in all other respects). A value of $\delta_{shift}=0.05\sigma$ was sufficient to observe both pole-vaulting and period slowdown [Fig. 7(c)]. This treatment was employed for all other investigations. The simulated values of a_{r_e}/a_r are shown in Fig. 8 as a function of the distance between the fiber center of mass and the bounding surface, d^{cm}. Experimental data from Refs. 21 and 23 are also included in the figure. The simulations agree fairly well with the experimental results.

It is tempting to ascribe the ability of a small value of δ_{shift} to reproduce experimental observations to an effect of fiber and wall surface roughness on the lubrication forces. Indeed, for real fiber diameters on the order of 10^{-5} m, $\delta_{shift}=0.05\sigma$ corresponds to a length scale of 500 nm, on the order of roughness dimensions for many surfaces. However, we note that our simulations only use an approximation to the many-body hydrodynamic problem, and our model fiber differs from real fibers, especially near the ends. At this stage, we can only state that fiber dynamics near a solid surface are sensitive to the nature of the wall interactions. More conclusive statements about the role of surface roughness require more realistic fiber model shapes, and more accurate treatments of the short-range forces.

Depending on the initial orbit constant and center of mass, the fibers pole-vault into orbits with larger or smaller orbit constants. The displacement of the center of mass away from the wall is typically accompanied by a displacement in the vorticity direction. The lateral displacement was larger for fibers pole-vaulting into smaller orbit constants than those pole-vaulting into larger orbit constants. The displacement also increased with decreasing separation between the center of mass and the wall. Such effects have yet to be investigated experimentally, but could be of interest when considering fiber dynamics and suspension structure near walls.

The deviation in rotation rate in pole-vaulting simulations, relative to the same fiber in unbounded flow, is plotted as a function of ϕ in Fig. 9 ($C=\infty$). The fiber rotation rate decreases as it aligns with the flow, relative to that of a fiber in unbounded shear flow. This is consistent with Ingber and Mondy's[20] boundary element simulations of a spheroid in shear flow near both shearing surfaces. Although our simulated rotation rates, averaged over a period, indeed show an increase in the orbit period, the observed slowdown is nonuniform, in contrast to the experimental observations of Stover and Cohen[21]. The discrepancy may arise from our approximate hydrodynamic interactions, or from differences in the nonhydrodynamic interactions between the fiber and wall.

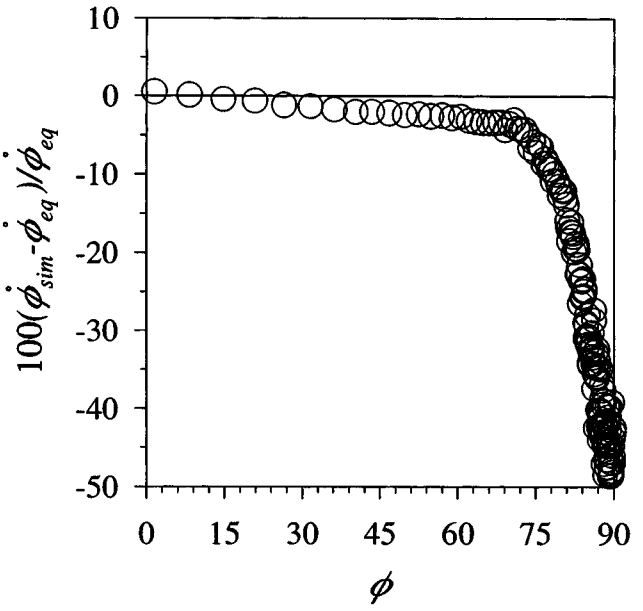

FIG. 9. Deviation of the rotation rate of a simulated fiber ($\dot{\phi}_{sim}$; $C=\infty$) from that predicted by Jeffery's analysis for the same equivalent aspect ratio ($\dot{\phi}_{eq}$). The fiber is aligned with the flow when $\phi=90°$.

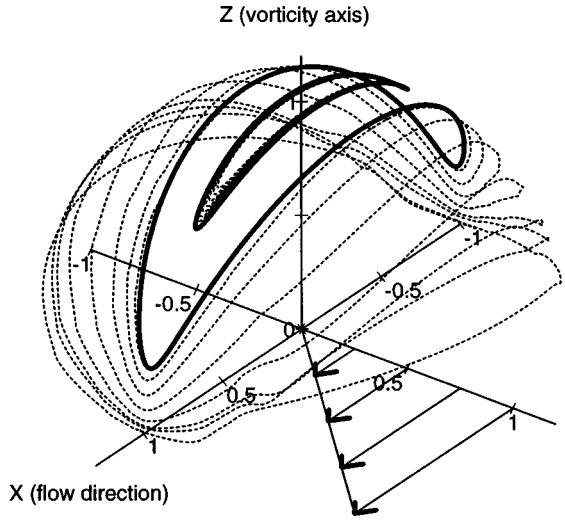

FIG. 10. Orbit trajectories for flexible fibers. For $C^0=0.2$, the fiber drifts toward the XY plane ($k^{(B)}*=30$). For $C^0=0.05$, the fiber drifts toward the Z axis ($k^{(B)}*=20$).

C. Flexible fibers

Flexible fibers exhibit more complicated dynamics than rigid fibers. In this section we restrict our attention to ideal flexible fibers in unbounded shear flows ($H/\sigma=25$), composed of $N=15$ spheres with $\kappa_1=\kappa_2=0.1$ ($a_r=17.8$), and varying $k^{(B)}*$ ($k^{(T)}*/k^{(B)}*=2/3$; $F_0^*=1.0$). We examine the orbital drift, the transient orbit period, and the classification of configurational dynamics.

1. Orbital drift

Recall the following main features of the rotation of rigid, axisymmetric particles: the orbits are stable, and the dimensionless period $T\dot{\gamma}$ does not depend on C or $\dot{\gamma}$. In contrast, we find that flexible fiber orbits are, in general, not stable, and that $T\dot{\gamma}$ depends on both C and $\dot{\gamma}$.

Orbital drift is illustrated in Fig. 10, where the trajectory of the normalized fiber end-to-end vector is plotted in three dimensions for two different initial orientations. These simulations were started with straight fibers in the XZ plane, with an initial orbit constant C^0. For $C^0=0.05$, the orbit drifts slowly toward $C=0$ ($\lambda_{xz}=0$). For $C^0=0.2$, the orbit drifts more rapidly toward $C=\infty$ ($\lambda_{xz}=90°$), approaching an orbit entirely within the XY plane. This is consistent with the experimental observations of Arlov *et al.*[9] who reported a tendency for fiber orbits to drift toward $C=0$ or ∞, with intermediate values occasionally observed.

The concept of orbit constants is ill-defined for flexible fibers whose geometries vary with time. We characterize the orbital drift for flexible fibers with the rock angle λ_{xz}, defined as the angle between the fiber end-to-end vector and the Z axis, as the end-to-end vector passes through the XZ plane. This is equivalent to the definition employed by Arlov *et al.*[9] Apparent orbit constants can then be defined using Eq. (4) with an equivalent aspect ratio. Although the meaning of this orbit ''constant'' is unclear for a flexible fiber, it does serve to discriminate between orbits lying nominally in the XY plane ($C\gg1$) and those fibers rotating with their major axes near the Z axis ($C\ll1$).

The orbital drift of fibers with different $k^{(B)}*$ is illustrated in Figs. 11(a) and 11(b) for simple and parabolic shear flows, respectively, where the rock angle λ_{xz} is plotted as a function of the rotation period. Again, simulations were started with the fiber straight in the XZ plane. For $k^{(B)}*\leqslant50$ in simple shear flow, the fibers drifted toward one of two preferred orientations. For $C^0<0.06$, fibers drifted toward smaller C; for $C^0>0.1$, fibers drifted toward larger C. For all C^0, the drift rate increases with decreasing $k^{(B)}*$. Drift toward smaller C ($C^0<0.06$) is slower than the drift toward larger C. This dependence of drift rate on stiffness and drift direction was also observed by Arlov *et al.*[9]

The strong correlation between drift rate and stiffness is expected, since rigid fibers should not drift. Flexible fibers at large C experience large axial hydrodynamic forces, and the resulting deformations allow the orbit to drift. Fibers at smaller C remain relatively straight, since the axial forces are smaller [Eq. (6)], and the drift rate is therefore reduced.

Arlov *et al.*[9], however, found that the fibers drifted to their ultimate orientations faster than we observe in the simulations—within 1 period for larger orbit constants, and within about 20 periods for smaller orbit constants. The differences between their observations and our simulations may arise from differences in fiber flexibility, aspect ratio [Arlov *et al.* employed fibers with $a_r\sim\mathcal{O}(10^2)$], or shear rate. Determining drift rates for large aspect ratios is computationally expensive (when the beads are spheres), and thus is postponed for future publications.

Fibers in simple shear flow that drift toward larger C do not drift completely into the XY plane [Fig. 11(a)]. As discussed below, the orbit fluctuations near $\lambda_{xz}=90°$ are asso-

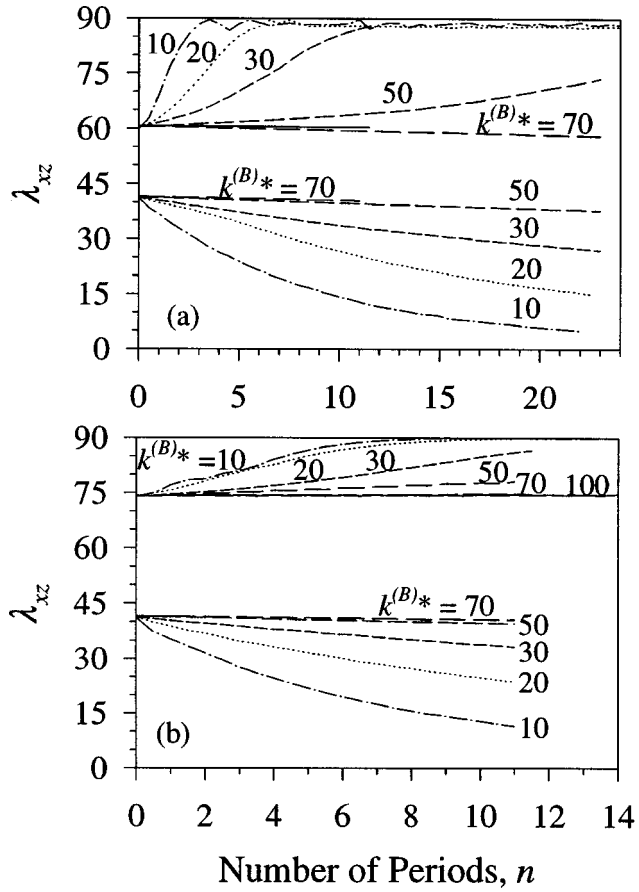

FIG. 11. Rock angle, λ_{xz}, as a function of the number of rotation periods for flexible fibers in (a) simple shear and (b) parabolic shear flow. (a) The top part of the figure is for an initial orientation of $C^0=0.1$, where the fibers drift to larger orbit constants. The solid line is for a simulation with $k^{(B)}*=2500$. The lower part of the figure is for an initial orientation of $C^0=0.05$, where the fibers drift to smaller orbit constants. (b) The top part of the figure is for an initial orientation of $C^0=0.2$, where the fibers drift to larger orbit constants. The lower part of the figure is for an initial orientation of $C^0=0.05$, where the fibers drift to smaller orbit constants.

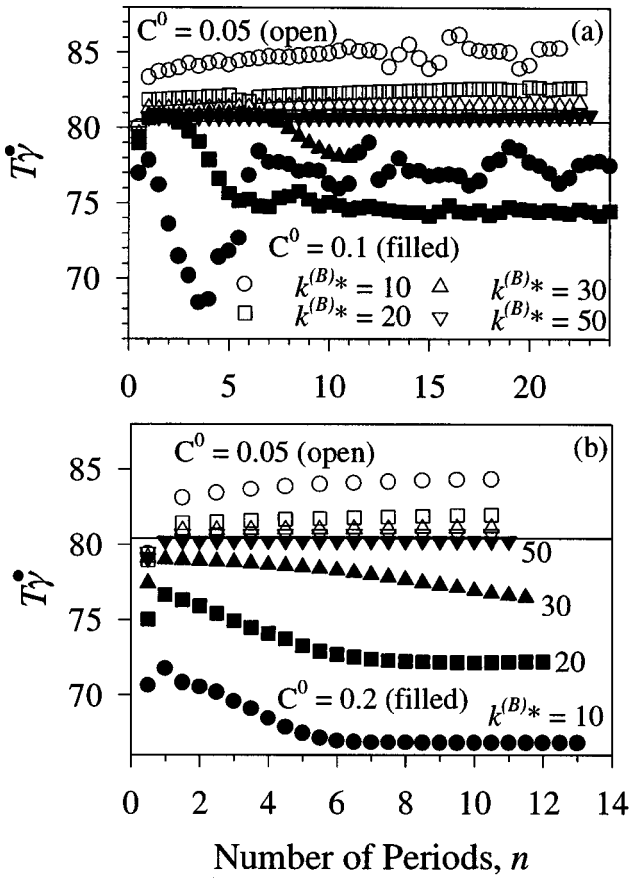

FIG. 12. Dimensionless orbit period, $T\dot{\gamma}$, as a function of the number of rotation periods for fibers with various flexibilities in (a) simple shear and (b) parabolic shear flow. The solid horizontal lines indicate the dimensionless period for a rigid fiber.

ciated with flexing motions of the fibers. For fibers with $50<k^{(B)}*<200$ in simple shear flow, the dynamics and drift depend on $k^{(B)}*$ as well as C^0. For some intermediate orbits with large C^0, some fibers drift toward smaller C, but then remain indefinitely at an intermediate value.

Stiffer fibers ($k^{(B)}*\geqslant 200$) rotate like rigid rods when $C^0=\infty$, and exhibit very slow drift for finite values of C^0. For $k^{(B)}*=2500$ and $C^0=0.1$, the drift in λ_{xz} is less than 0.28° during the first 10 periods, which may in part be due to round-off error. Although fibers with $k^{(B)}*=\infty$ have not been simulated, the trend clearly suggests that fibers appear to rotate in stable orbits in the limit as $k^{(B)}*\rightarrow\infty$.

Flexible fibers in parabolic shear flow exhibited similar trends, with a few exceptions [Fig. 11(b)]. For $k^{(B)}*<50$, fibers with $C^0<0.1$ and $C^0>0.2$ drift toward smaller and larger C, respectively. Fibers that drift toward larger C drift completely into the XY plane ($\lambda_{xz}=90°$). Thus, in contrast to the predictions by Chwang[7] for rigid prolate spheroids, flexible fiber dynamics depend on the ambient flow.

The dependence of drift on $k^{(B)}*$ and C^0 is summarized in Table II for fibers in simple and parabolic shear flows.

2. Orbit period

$T\dot{\gamma}$ is plotted as a function of the number of periods in Figs. 12(a) and 12(b) for simple and parabolic shear flows, respectively, for fibers with different stiffnesses and initial orientations. Several general trends for the behavior as $t\rightarrow\infty$ are discernible. Dimensionless periods for large C are smaller than those of rigid fibers, and they decrease with decreasing $k^{(B)}*$. This is consistent with the observation for rigid fibers that $T\dot{\gamma}$ decreases with decreasing aspect ratio—the effective aspect ratio of a flexible fiber bent in the XY plane is smaller than its nominal value. Fibers at small C have dimensionless periods larger than those of rigid fibers, which increase with decreasing $k^{(B)}*$.

During drift, $T\dot{\gamma}$ does not always vary monotonically with time, especially for fibers drifting toward larger C in simple shear [Fig. 12(a)], and those that settle into intermediate orbit constants. For $C^0=0.1$, a fiber with $k^{(B)}*=50$ in simple shear drifts slowly toward $C=\infty$ [Fig. 11(a)]. Although the trend suggests that its period will eventually decrease below that of a rigid fiber, $T\dot{\gamma}$ is still slightly greater

TABLE II. Dependence of drift on fiber orientation and flexibility, for fibers in simple shear flow (results for parabolic shear flow are given in parentheses). Symbols: ↑—the fiber drifted to larger orbit constants; ↓—the fiber drifted to smaller orbit constants; ×—the fiber settled in an intermediate orbit, or no drift occurred ($C=\infty$).

	Bending stiffness $k^{(B)}*$					
C^0	10	20	30	50	70	100
∞	×(×)	×(×)	×(×)	×(×)	×(×)	×(×)
0.5	↑(↑)	↑(↑)	↑(↑)	↑(↑)	×(↓)	↓
0.2	↑(↑)	↑(↑)	↑(↑)	↑(↑)	↑(↑)	↓(↑)
0.1	↑(↓)	↑(↓)	↑(↓)	↑(↓)	↓(×)	↑
0.06			↓			
0.05	↓(↓)	↓(↓)	↓(↓)	↓(↓)	↓(↓)	↓
0.01	↓		↓			

than that of a rigid fiber after 20 periods. The larger intermediate period is consistent with a finite intermediate orbit constant.

More complex transients are observed for flexible fibers with $k^{(B)}*=10$ and $C^0=0.1$ in simple shear flow. The fiber rapidly drifts toward $C=\infty$, although never drifting completely into the XY plane [Fig. 11(a)]. $T\dot{\gamma}$ fluctuates significantly with time as it drifts [Fig. 12(a)]. Such fluctuations are associated with complex configurational dynamics, discussed below. For fibers drifting toward $C=\infty$ in parabolic shear flow, the limiting periods are identical to those of fibers initially in the XY plane.

3. Classification of configurational dynamics

Configurational dynamics observed for flexible fibers can be described in terms of the classifications defined by Arlov *et al.*[9] Examples of various orbits are illustrated in Figs. 13–17, where snapshots of the fiber projection onto the YZ, XZ, and XY planes are shown during one half of an orbit, with time increasing from left to right.

Flexible fibers with small C exhibit flexible spin-rotation orbits (Group 2) for both simple and parabolic shear flow. Deformation is minimal, as expected, since axial hydrodynamic forces are small. Furthermore, for such fibers rotating with small orbit constants, the extent of deformation depends only weakly on λ_{xz} and $k^{(B)}*$. We have not observed Group 1 dynamics (flexible spin) for the range of flexibilities and the aspect ratio investigated.

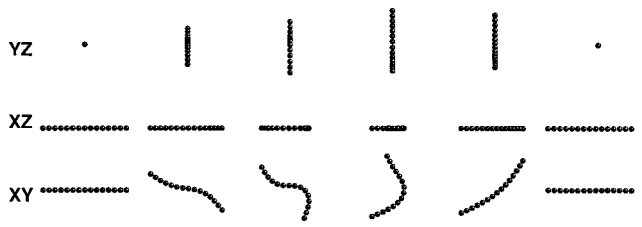

FIG. 13. Springy rotation (Group 3A) configurational dynamics exhibited by relatively stiff fibers ($k^{(B)}*=70$) rotating in $C=\infty$ orbits. These snapshots (as well as those in following figures) are for the last half-period in a simulation to a shear strain of 1900 (evaluated at the fiber center of mass). The behavior, depicted here for simple shear flow, is the same in simple and parabolic shear flows.

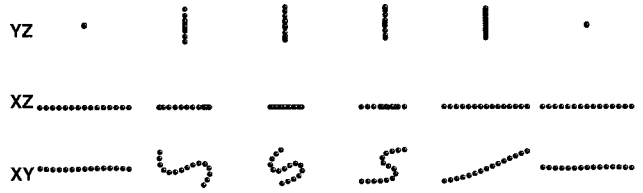

FIG. 14. Pure S-turn (Group $3C_2$) configurational dynamics exhibited by relatively flexible fibers ($k^{(B)}*=20$) rotating in $C=\infty$ orbits. The behavior, depicted here for parabolic shear flow ($C^0=0.5$), is the same in simple and parabolic shear flows.

Fibers initially in the XY plane ($C^0=\infty$) exhibit springy rotations (Group 3A, Fig. 13) or pure S-turns (Group $3C_2$, Fig. 14), with a gradual transition from the latter to the former as $k^{(B)}*$ increases from about 50 to 70. These motions were observed for both simple and parabolic shear flow.

More complex dynamics are observed for fibers as they drift toward larger orbit constants in simple shear flow. The results for this category are summarized in Table III. Recall that these fibers do not drift completely into the XY plane, and the value of λ_{xz} fluctuates in time. Very flexible fibers ($k^{(B)}*=10,20,30$) drift rapidly toward the XY plane, exhibiting S-loopturn rotations (Group $3C_1$; Fig. 15). Fibers with intermediate flexibilities ($k^{(B)}*\approx 50$) eventually rotate through U-turns (Group 3B; Fig. 16). U-turns were also observed during the initial periods for more flexible fibers that eventually display S-loopturns. However, the initial loopturns of the more flexible fibers are markedly sharper than those of stiffer fibers. Stiff fibers ($k^{(B)}*=70$) that settle into intermediate orbit constants display flexible spin rotations (Group 2; Fig. 17). The deformation in this case is much larger than that exhibited by flexible fibers that drift toward smaller C.

The fluctutations in λ_{xz} with time for fibers approaching $C=\infty$ in simple shear flow [Fig. 11(a)] are associated with fluctuations in the transient configurations; the fibers do not repeat the same motion precisely through each rotation. These fluctuations persist for at least 20 full periods. Whether or not these dynamics reach a steady-state is not clear.

IV. CONCLUSION

In this paper, we presented simulation results for the motion of flexible fibers modeled as rigid spheres connected

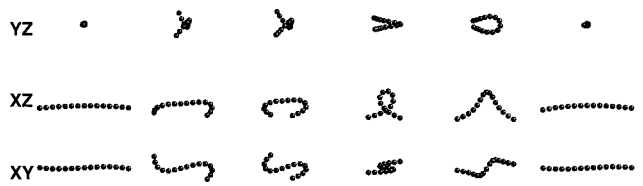

FIG. 15. S-loopturn (Group $3C_1$) configurational dynamics exhibited by very flexible fibers ($k^{(B)}*=10$, $C^0=0.5$) drifting toward $C=\infty$ orbits in simple shear flow. In parabolic shear flow, such a fiber drifts entirely into the XY plane, exhibiting pure S-turns.

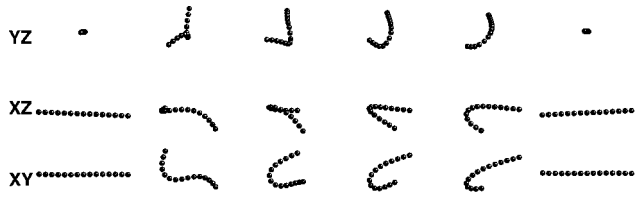

FIG. 16. U-turn (Group $3B$) configurational dynamics exhibited by flexible fibers ($k^{(B)}*=50$, $C^0=0.5$) drifting toward $C=\infty$ orbits in simple shear flow.

TABLE III. Classification of flexible fiber dynamics for fibers in simple shear flow, with different initial orientations and stiffnesses. All fibers with these stiffnesses and initial orientations drifted to larger orbit constants with $\lambda_{xz}\simeq 90°$. The different classes of dynamics are described in the text.

Group	$C^0=0.1$	$C^0=0.2$	$C^0=0.5$	$C^0=\infty$
2		70	70	
3A				70 → 200
3B	30, 50	50	50	
$3C_1$	10, 20, 30	10, 20, 30	10, 20,30	
$3C_2$				10,20,30,50

by ball and socket joints. Resistance to bending and twisting was included through potentials prescribed in the joints. The purposes of this paper were to verify that this model accurately reproduces known results for fiber dynamics, and to illustrate the complicated dynamics of flexible fibers.

Simulations of isolated stiff fibers reproduced such features of Jeffery orbits as orbit stability, the dependence of $T\dot{\gamma}$ on only the a_r (independent of $\dot{\gamma}$ and C), and trajectories identical to those of prolate spheroid of the same equivalent aspect ratio. Orbit periods were unchanged in parabolic shear flow, as predicted by Chwang[7].

Simulations of stiff fibers pole-vaulting near a bounding surface qualitatively reproduced experimental observations of Stover and Cohen[21]. Fiber trajectories are very sensitive to the short-range interactions between a fiber and a bounding surface. This suggests that very detailed knowledge and modeling of the fiber shape (especially at the ends) and interactions are required to quantitatively reproduce experimental observations.

In contrast to rigid fibers, flexible fiber orientations drift in simple and parabolic shear flows. Fibers at relatively small C^0 drift toward $C=0$, while fibers at relatively large C^0 drift toward $C=\infty$. The drift direction and rate depends on $k^{(B)}*$, C^0 orientation, as well as the ambient flow field. A wide variety of configurational dynamics are observed, which also depend on $k^{(B)}*$, C^0, and the ambient flow field. These results agree with the experimental observations of Arlov *et al.*[9]

Hydrodynamic interactions between the beads within a fiber were neglected in this study to reduce computation time. Including them will certainly quantitatively alter the results. Interestingly, simulations of rigid fibers reproduce almost all aspects of isolated rigid fiber motion when these interactions are neglected. Hydrodynamic interactions are apparently only required to accurately determine the orbit period, or equivalently, the equivalent fiber aspect ratio. The influence of hydrodynamic interactions on flexible fiber dynamics is unknown.

Hydrodynamic interactions are but one feature that has been neglected in this study. Real fibers, especially wood pulp fibers, are often not straight (permanently deformed), their stiffnesses are not uniform along the contour, their cross-sections are not circular or uniform, and they can have fibrils and other asperities extending from their surfaces. Each of these features will influence flexible fiber dynamics to some extent, and each must be examined to accurately describe the behavior of real fibers.

Flexible fiber dynamics have practical relevance in several areas, and the results presented here help to illustrate how flexibility can impact processes. Fiber flocculation (e.g., in wood fiber suspensions) arises from fiber entanglement in flowing liquids[24,25]. The aggregate strength is believed to be dominated by the elastic forces exerted by deformed fibers within the flocs[26–29]. Fiber collisions, entanglement, and deformation within flocs will certainly depend on fiber conformational dynamics. The properties of fiber reinforced composites depend on the fiber orientations, which have been shown here to depend on such variables as fiber flexibility. Simulation methods are attractive tools for studying such problems, where configurational complexities effectively prohibit analytical treatments.

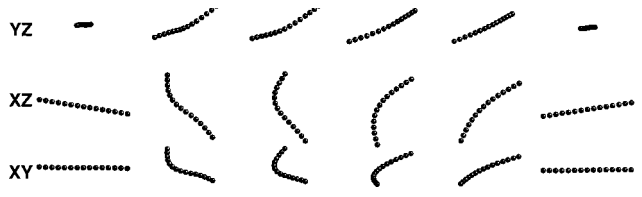

FIG. 17. Flexible spin-rotation (Group $3B$) configurational dynamics exhibited by relatively stiff fibers ($k^{(B)}*=70$, $C^0=0.5$) that settle into intermediate orbits in simple shear flow.

ACKNOWLEDGMENTS

P.S. acknowledges the financial support from the Norwegian Research Council Grant No. 100573/410, a NATO travel grant, and the generous use of the computer facilities of Professor F. Mo, Department of Physics, NTNU. R.F.R. and D.J.K acknowledge the support of the TAPPI Foundation and the National Science Foundation (Grant No. CTS-9502276).

[1] R. F. Ross and D. J. Klingenberg, J. Chem. Phys. **106**, 2949 (1997).
[2] G. B. Jeffery, Proc. R. Soc. London, Ser. A **102**, 161 (1922).
[3] B. J. Trevelyan and S. G. Mason, J. Colloid. Sci. **6**, 354 (1951).
[4] O. L. Forgacs and S. G. Mason, J. Colloid. Sci. **14**, 457 (1959).
[5] H. L. Goldsmith and S. G. Mason, *Rheology*, edited by F. R. Eirich, (Academic, New York, 1964), Vol. 4.
[6] F. P. Bretherton, J. Fluid Mech. **14**, 284 (1962).
[7] A. T. Chwang, J. Fluid Mech. **72**, 17 (1975).
[8] A. L. Yarin, O. Gottlieb, and I. V. Roisman, J. Fluid Mech. (accepted).

[9] A. P. Arlov, O. L. Forgacs, and S. G. Mason, Sven. Papperstidn. **61**, 61 (1958).
[10] O. L. Forgacs and S. G. Mason, J. Colloid. Sci. **14**, 473 (1959).
[11] S. Yamamoto and T. Matsuoka, J. Chem. Phys. **98**, 644 (1993).
[12] S. Yamamoto and T. Matsuoka, J. Chem. Phys. **100**, 3317 (1994).
[13] S. Yamamoto and T. Matsuoka, Polym. Eng. Sci. **35**, 1022 (1995).
[14] S. Yamamoto and T. Matsuoka, J. Chem. Phys. **102**, 2254 (1995).
[15] J. Wittenburg, *Dynamics of Systems of Rigid Bodies* (B.G. Teubner Stuttgart, 1977), ISBN 3-519-02337-7.
[16] S. Kim and S. J. Karrila, *Microhydrodynamics: Principles and Selected Applications* (Butterworth–Heinemann, Boston, 1991), ISBN 0-7506-9173-5.
[17] J. Happel and H. Brenner, *Low Reynolds Number Hydrodynamics* (Kluwer Academic, Dordrecht, 1991), ISBN 90-2472877-0.
[18] R. G. Cox, Int. J. Multiphase Flow **1**, 343 (1971).
[19] J. M. Burgers, in *Second Report on Viscosity and Plasticity* (North-Holland, Amsterdam, 1938), Chap. 3.
[20] M. S. Ingber and L. A. Moundy, J. Rheol. **38**, 1829 (1994).
[21] C. A. Stover and C. Cohen, Rheol. Acta **29**, 192 (1990).
[22] G. Bossis and J. F. Brady, J. Chem. Phys. **80**, 5141 (1984).
[23] H. L. Goldsmith and S. G. Mason, J. Colloid. Sci. **17**, 448 (1962).
[24] S. G. Mason, Pulp Paper Mag. Can. **49**, 93 (1948).
[25] S. G. Mason, Tappi J. **37**, 494 (1954).
[26] R. Meyer and D. Wahren, Sven. Papperstidn. **67**, 432 (1964).
[27] R. M. Soszynski and R. J. Kerekes, Nordic Pulp Pap. Res. J. **3**, 172 (1988).
[28] R. R. Farnood, S. R. Loewen, and C. T. J. Dodson, APPITA J. **47**, 391 (1994).
[29] S. Toll and J. A. E. Manson, J. Appl. Mech. **62**, 223 (1995).